PTEP

Prog. Theor. Exp. Phys. **2015**, 03A104 (15 pages)
DOI: 10.1093/ptep/ptu069

PHYSICS at PHENIX, 15 years of discoveries

Soft physics results from the PHENIX experiment

ShinIchi Esumi*,†

Institute of Physics, University of Tsukuba, Tenno-dai 1-1-1, Tsukuba, Ibaraki 305-8571, Japan
*E-mail: esumi.shinichi.gn@u.tsukuba.ac.jp

Received March 30, 2014; Accepted April 30, 2014; Published January 12, 2015

High-energy heavy-ion collisions at RHIC-BNL and LHC-CERN provide a unique opportunity to study the properties of the high-temperature and high-density nuclear matter called the quark–gluon plasma (QGP), which is supposed to exist in the early universe or inside neutron stars. The PHENIX experiment is one of the major experiments at RHIC to study the properties of QGP, especially focusing on various particle identification capabilities including photons, leptons, and hadrons. This article summarizes the soft physics results from the PHENIX experiment, such as (1) global properties like transverse energy and multiplicity measurements as well as centrality determination, (2) transverse momentum distribution and the nuclear modification factor, which represents the modification of the spectra in $A + A$ collisions relative to the binary-collision-scaled superposition of p+p data, (3) space-time properties with Hanbury Brown and Twiss (HBT) interferometry correlation measurement and source imaging, (4) elliptic collective expansion and higher-order harmonic event anisotropy, and (5) di-hadron correlation, jet modification, and medium response known as jet-quenching from the partonic energy loss and redistribution of the lost energy. These results are reviewed and discussed.

Subject Index D28, D30, D31, D33

Contents

1. Transverse energy, multiplicity measurement, and centrality

High-energy heavy-ion collisions are characterized by the centrality that is given by the impact parameter, which is the nearest distance between two colliding nuclei perpendicular to the beam direction. In order to quantify the centrality, which controls the geometrical shape and volume of

†Many thanks to the PHENIX Collaboration.

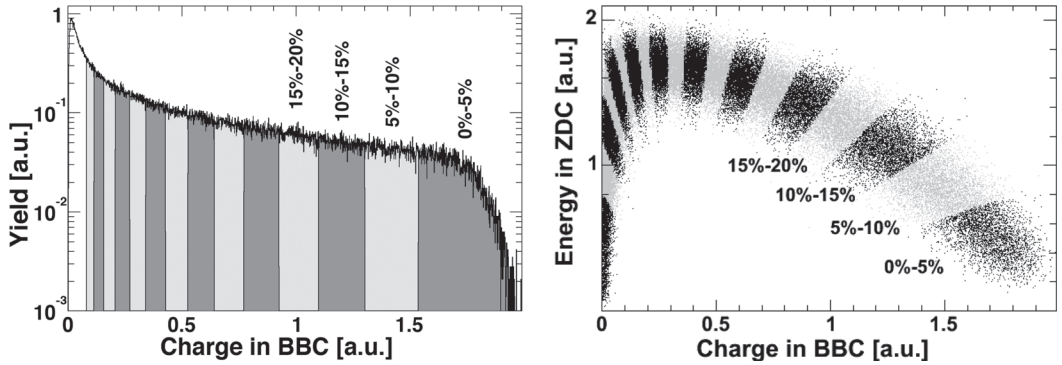

Fig. 1. Charged particle multiplicity distribution in BBC (left) and correlation between spectator neutron energy in ZDC and charged particle multiplicity in BBC (right) are shown with centrality definitions [1].

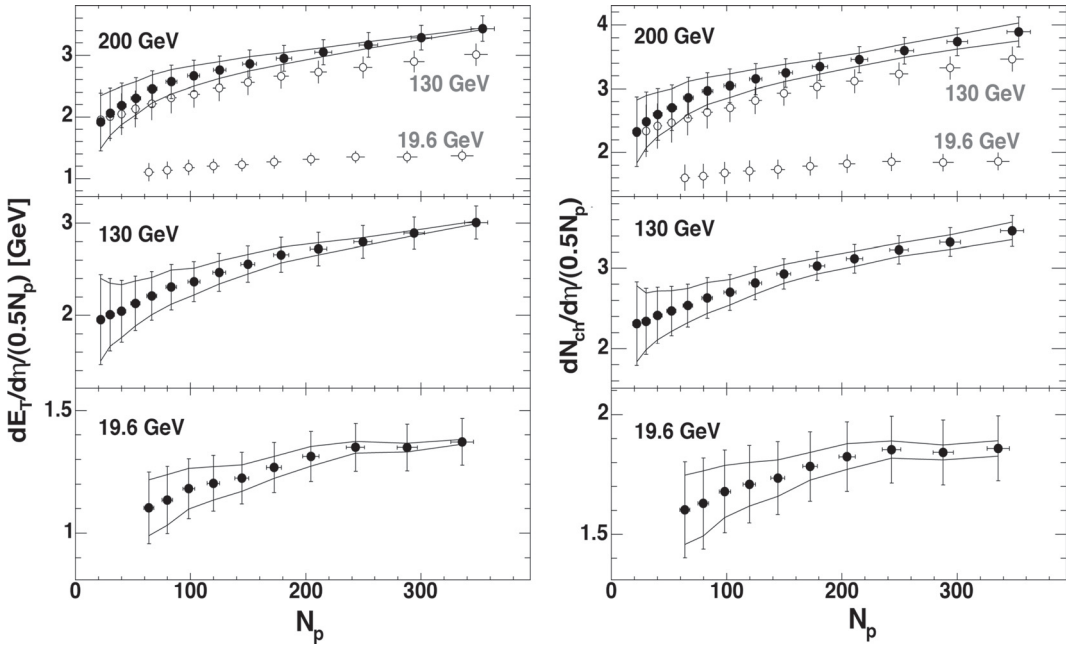

Fig. 2. Transverse energy and charged particle multiplicity per unit η per participant pair are shown as a function of the number of participants $N_{\rm p}$ at $\sqrt{s_{NN}} = 200$, 130, and 19.6 GeV Au + Au collisions [1].

the participant region for a given nucleus–nucleus collision, the charged particle multiplicity in the two forward beam–beam counters (BBC) at $|\eta| = 3$–4 are used to determine the collision centrality in the PHENIX experiment based on the Glauber simulation including the detector response. The left panel in Fig. 1 shows an arbitrary normalized charged particle multiplicity distribution in the BBC detector with a 5% centrality step, where the centrality of 0% corresponds to the most central interactions. The right panel in Fig. 1 shows the correlation between the neutron energy of a spectator nucleus measured by the zero-degree calorimeter (ZDC) and the charged particle multiplicity in the participant region, where a clear anti-correlation between the spectator neutron energy and the participant charged particle multiplicity can be seen in the central to mid-central collisions, while the spectator neutron energy is reduced for the peripheral collisions due to the reduced efficiency of the spectator break-up in order for the neutrons to be observed in the ZDC [1].

The transverse energy per unit η per participant pair $(dE_{\rm T}/d\eta)/(0.5N_{\rm p})$ is shown as a function of the number of participants $N_{\rm p}$ in the left panels of Fig. 2 for three different colliding beam energies

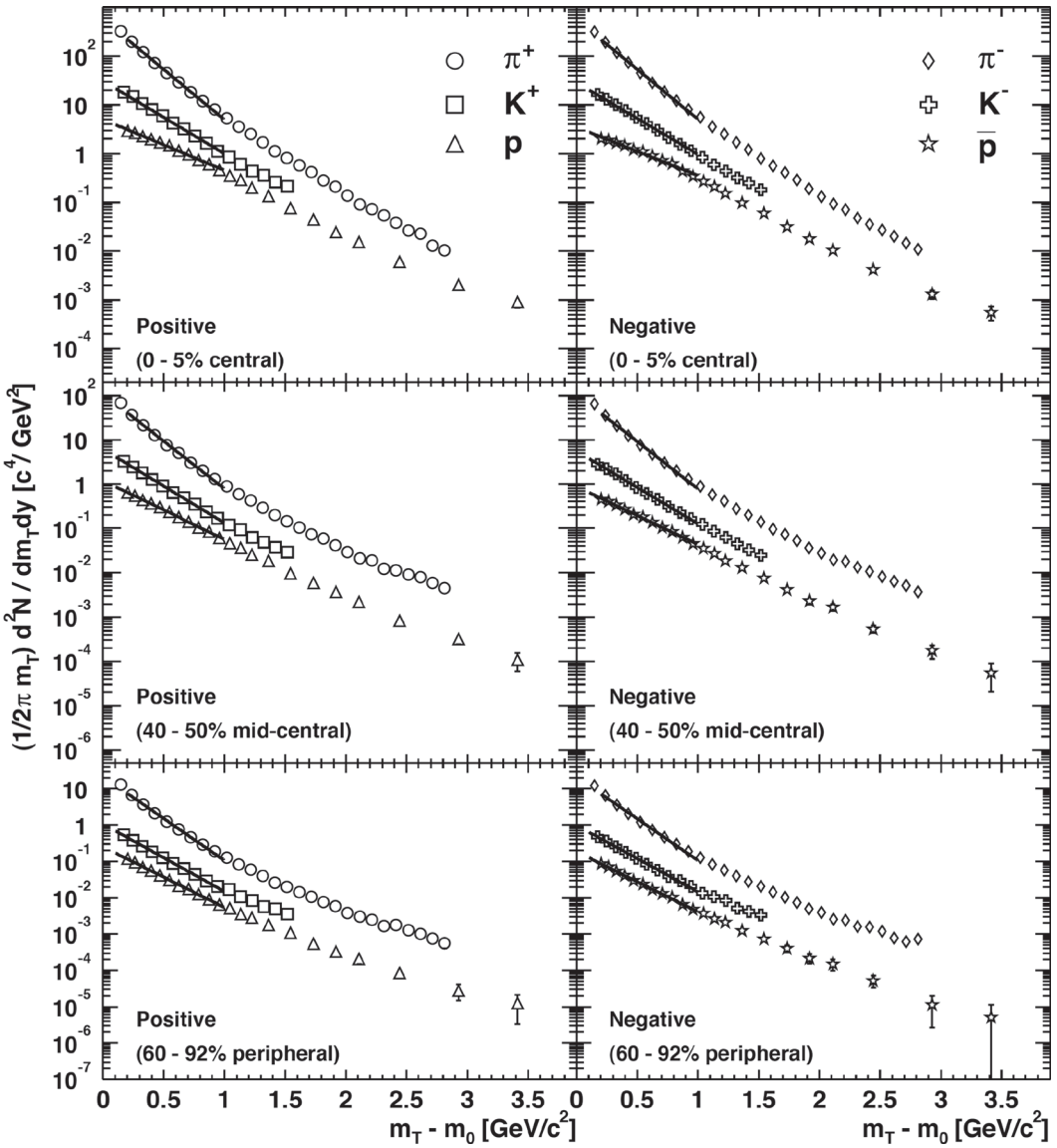

Fig. 3. Transverse mass m_{T} spectra for $\pi^{\pm}$, $\mathrm{K}^{\pm}$, p, and $\bar{\mathrm{p}}$ in $\sqrt{s_{NN}} = 200\,\mathrm{GeV}$ Au + Au collisions [2]. The lines on each spectra are m_{T} exponential functions at 0.2–1.0 GeV/c^2 for $\pi^{\pm}$ and 0.1–1.0 GeV/c^2 for $\mathrm{K}^{\pm}$, p, and $\bar{\mathrm{p}}$.

of $\sqrt{s_{NN}} = 200$, 130, and 19.6 GeV Au + Au collisions. The charged particle multiplicity per unit η per participant pair $(dN_{\mathrm{ch}}/d\eta)/(0.5N_{\mathrm{p}})$ is shown in the right panels of Fig. 2, where very similar centrality dependences for both the transverse energy and the charged particle multiplicity are observed, indicating that the ratio of transverse energy per charged particle is almost independent [1].

2. Transverse momentum spectra and nuclear modification factor

Transverse momentum distributions for $\pi^{\pm}$, $\mathrm{K}^{\pm}$, p, and $\bar{\mathrm{p}}$ as a function of $m_{\mathrm{T}} - m_0$ are shown for positive particles in the left panels, for negative particles in the right panels, and for three centrality bins 0–5%, 40–50%, and 60–92% from the top to bottom panels of Fig. 3 in $\sqrt{s_{NN}} = 200\,\mathrm{GeV}$ Au + Au collisions [2]. The lines on each spectra are m_{T} exponential functions, where the fitted inverse slope parameter increases with particle mass as well as collision centrality, which indicates a

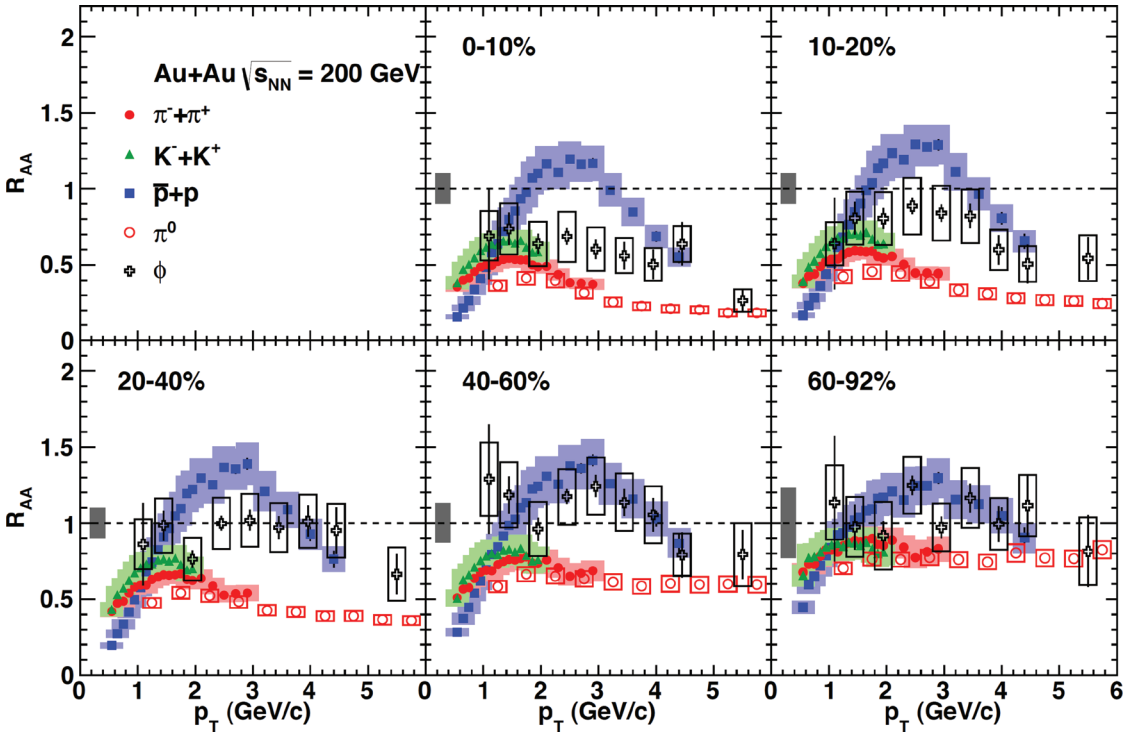

Fig. 4. Nuclear modification factor R_{AA} of $\pi^+ + \pi^-$, $\mathrm{K}^+ + \mathrm{K}^-$, $\mathrm{p} + \bar{\mathrm{p}}$, π^0, and ϕ as a function of p_{T} in $\sqrt{s_{NN}} = 200\,\mathrm{GeV}$ Au + Au collisions [3].

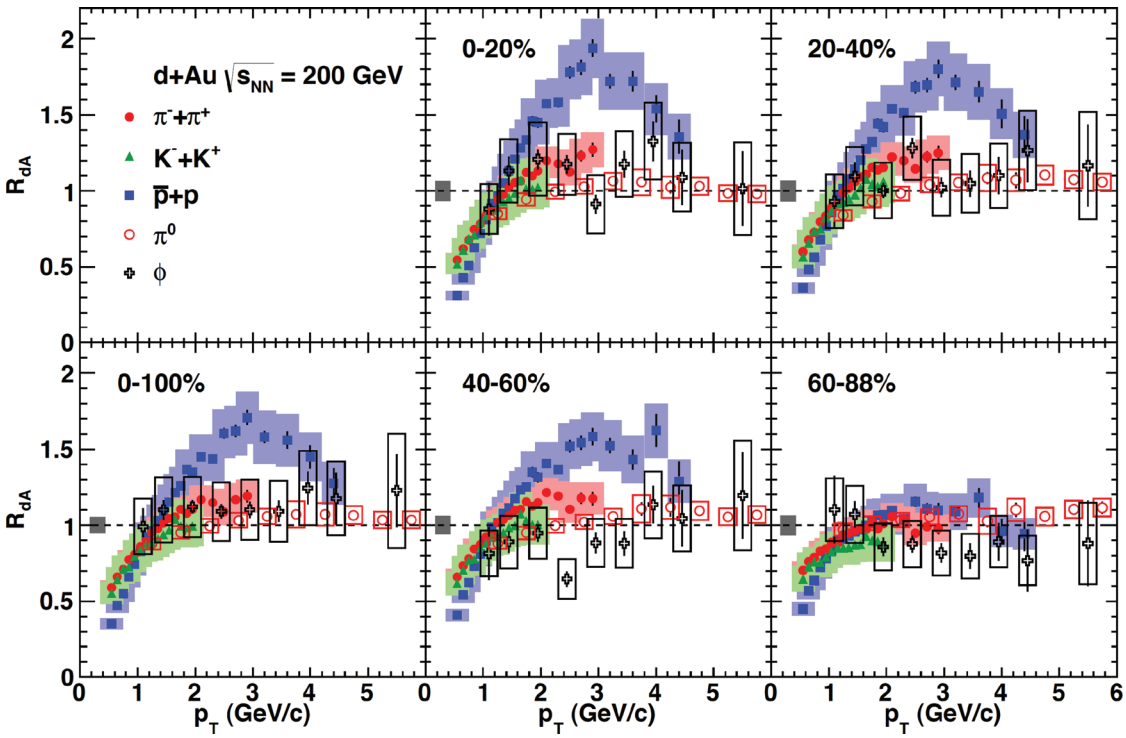

Fig. 5. Nuclear modification factor R_{dAu} of $\pi^+ + \pi^-$, $\mathrm{K}^+ + \mathrm{K}^-$, $\mathrm{p} + \bar{\mathrm{p}}$, π^0, and ϕ as a function of p_{T} in $\sqrt{s_{NN}} = 200\,\mathrm{GeV}$ d + Au collisions [3].

strong collective radial expansion, especially in central collisions. This has been very well described by hydrodynamic models.

The transverse momentum distributions of $\pi^+ + \pi^-$, $K^+ + K^-$, $p + \bar{p}$, π^0, and ϕ in $\sqrt{s_{NN}} =$ 200 GeV Au + Au collisions are normalized by the number of binary-collision-scaled superposition of spectra from p–p collisions at the same beam energy, which is defined as the nuclear modification factor R_{AA}, and are plotted as a function of transverse momentum p_T for 5 different centrality bins in Fig. 4 at $\sqrt{s_{NN}} = 200$ GeV Au + Au collisions [3]. The $\pi^+ + \pi^-$, π^0 are found to be strongly suppressed above 3 GeV/c, which is commonly attributed to jet suppression from partonic energy loss in the quark–gluon plasma (QGP), while $p + \bar{p}$ spectra are found to be almost scaled by the number of binary collisions or rather enhanced in the mid-p_T region around 2–4 GeV/c. This can be understood by hydrodynamic collective radial expansion as well as the quark coalescence model as the hadronization mechanism with radially expanding QGP.

The nuclear modification factor R_{dAu} of $\pi^+ + \pi^-$, $K^+ + K^-$, $p + \bar{p}$, π^0, and ϕ is shown as a function of p_T for 5 different centrality bins in Fig. 5 at $\sqrt{s_{NN}} = 200$ GeV d + Au collisions [3]. All the mesons are more or less binary scaled at higher p_T, while $p + \bar{p}$ are clearly enhanced above the binary scaling in the mid-p_T region around 2–4 GeV/c, which is also similar to Fig. 4 for Au + Au collisions.

3. HBT correlation and source imaging

Two-particle Hanbury Brown and Twiss (HBT) interferometry measurements are done with $\pi\pi$ and KK pairs at $\sqrt{s_{NN}} = 200$ GeV Au + Au collisions. The centrality and transverse momentum dependence of the radius parameters are shown as a function of $N_{part}^{1/3}$ and m_T in left and right panels in Fig. 6, respectively. The radius parameters for both $\pi\pi$ and KK pairs show a linear trend with $N_{part}^{1/3}$, which gives the length scale of the source, since N_{part} corresponds to the initial volume of the source. The radii from the KK pairs show smaller values compared to $\pi\pi$; however, the difference is mainly explained by m_T, where the reduction of radii as a function of transverse momentum of the pair also indicates the hydrodynamic collective expansion of the system before freeze-out. The ratio of R_{out}/R_{side} being about 1 usually means a short duration time (sudden freeze-out) in the case of a non-expanding static source; however, this is strongly affected by the collective expansion as well as the opacity of the source [4].

The model-independent source functions of the charged π emission region are extracted by the source-imaging method and shown in the left panels of Fig. 7 at $\sqrt{s_{NN}} = 200$ GeV Au + Au collisions. The corresponding measured correlation functions and imaged correlation functions are shown in the right panels of Fig. 7. The large difference between $S(r_x)$ and $S(r_y)$ indicates the long tail of the source geometry and emission duration, which is also given by the choice of the longitudinal center-of-mass system of the pair frame (LCMS) [5].

4. Elliptic flow and higher-order harmonic flow

The elliptic flow parameter v_2 in heavy-ion collisions has been observed to increase with colliding beam energy from AGS and SPS to RHIC, while the dependence at around $\sqrt{s_{NN}} = 62$–200 GeV is found to be rather weak, as shown in Fig. 8. In order to be less sensitive to the mean p_T, the data are compared at two different p_T regions of 0.65 GeV/c (closed symbols) and 1.75 GeV/c (open symbols). Therefore, the average v_2 could still increase, but $v_2(p_T)$ has be found to be almost unchanged between 62 and 200 GeV/c [6].

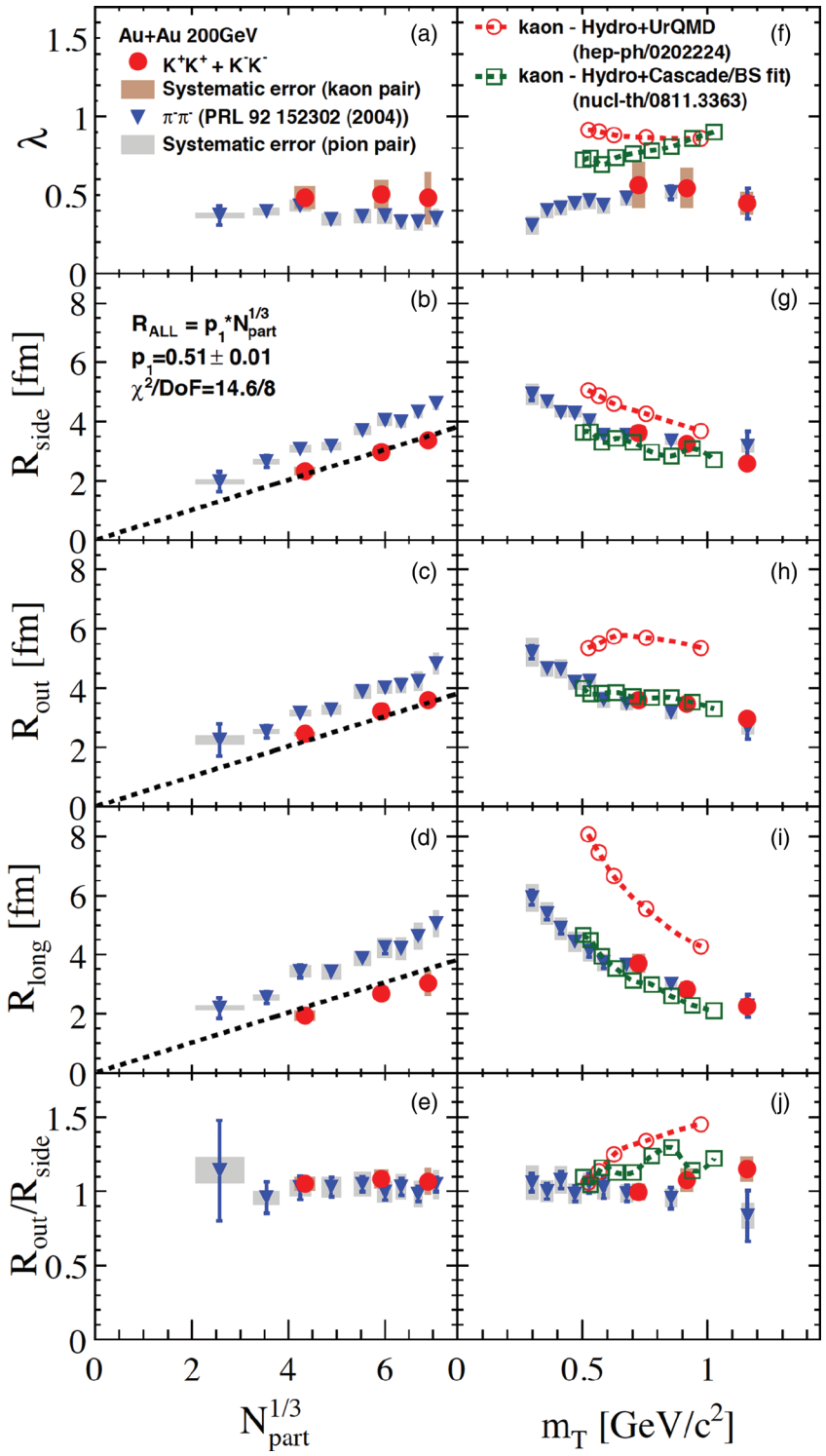

Fig. 6. HBT radius parameters with $\pi\pi$ and KK pairs as a function of $N_{\rm part}^{1/3}$ (left) and $m_{\rm T}$ (right) in $\sqrt{s_{NN}} = 200\,\text{GeV}$ Au + Au collisions [4].

The PHENIX experiment has used various different event-plane (E.P.) detectors in the forward rapidity region in order to measure v_2, v_4 at mid-rapidity with a large enough rapidity gap between particle and E.P. and to understand the non-flow effects, where the measured v_2 and v_4 parameters are shown for different choices of E.P. detectors in Fig. 9 as a function of $N_{\rm part}$ and $p_{\rm T}$

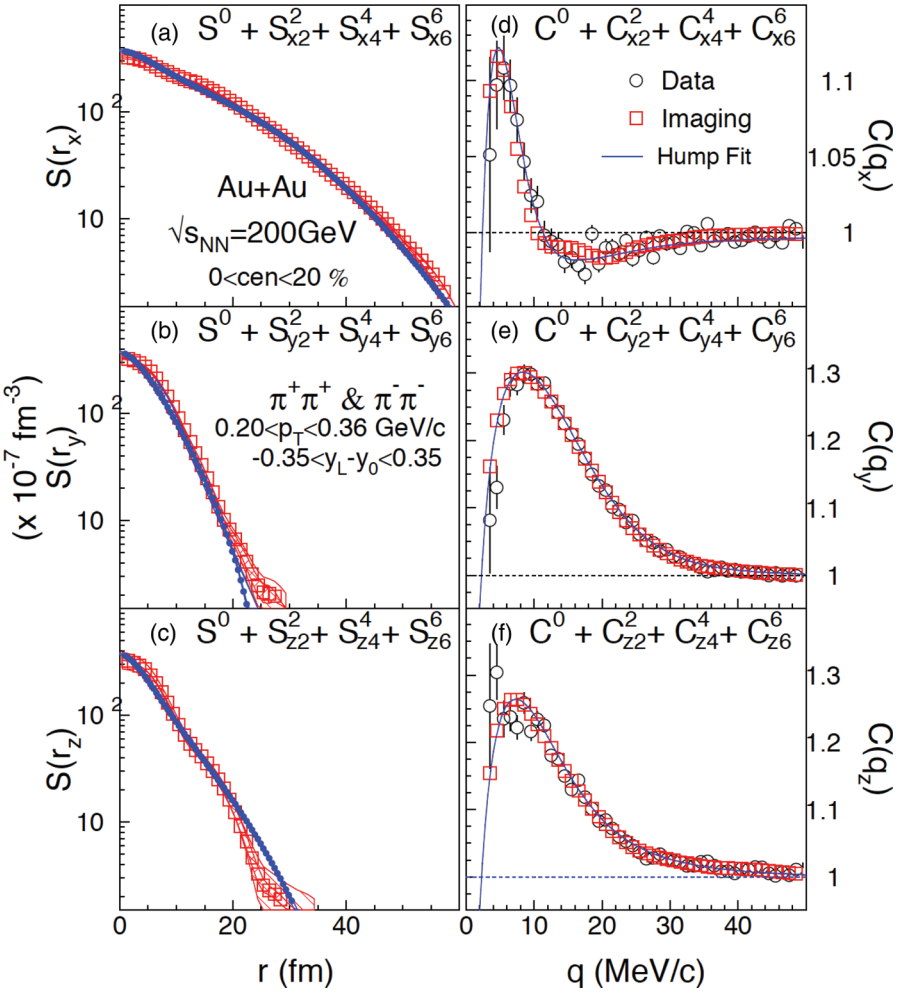

Fig. 7. Imaged sources (left), where the S(r_x) and S(r_y) correspond to the "out" and "side" directions and S(r_z) is for the "long" direction, and corresponding measured and imaged correlation functions (right) [5].

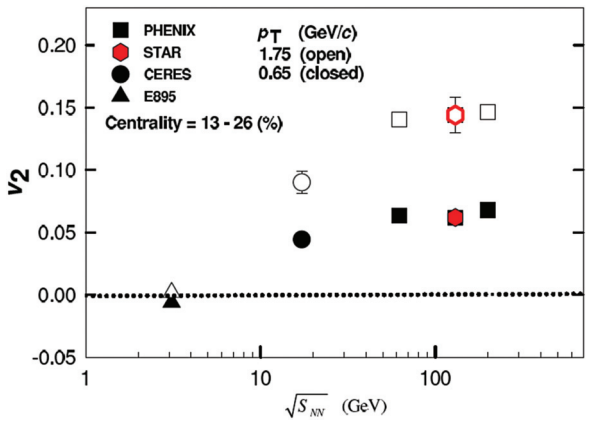

Fig. 8. Energy dependence of charged particle v_2 at two different p_T regions [6].

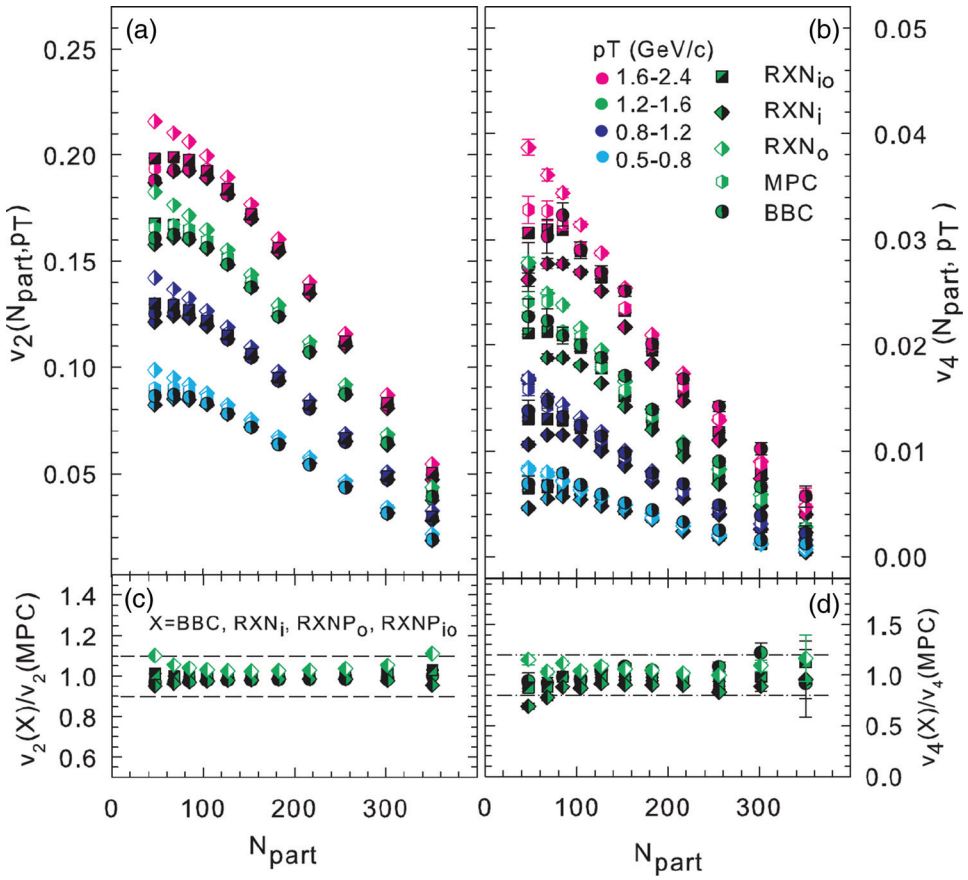

Fig. 9. $v_2\{\Psi_2\}$, $v_4\{\Psi_2\}$ with various E.P. detectors [7].

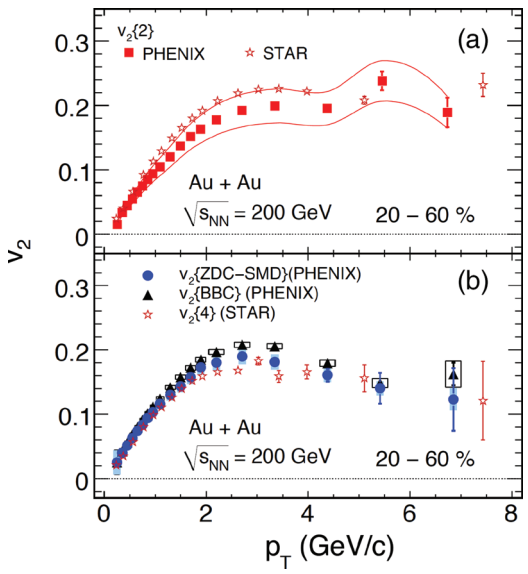

Fig. 10. v_2 with two- and four-particle cumulant methods and participant- and spectator-E.P. methods [8].

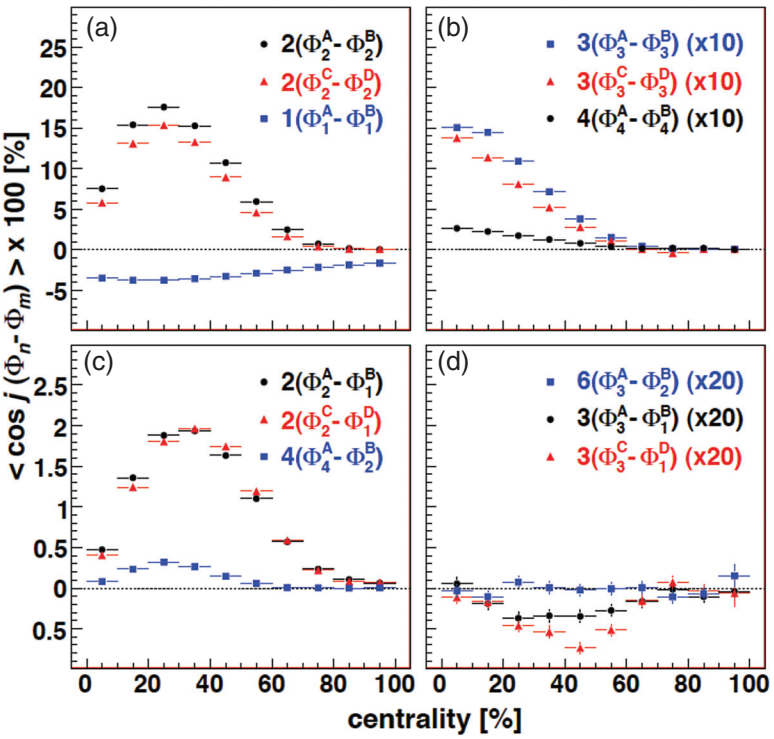

Fig. 11. Higher-order E.P. correlation. A: RXN^+, B: BBC^-, C: MPC^+, and D: MPC^-, where $+$ and $-$ are for the positive and negative rapidity regions, respectively [9].

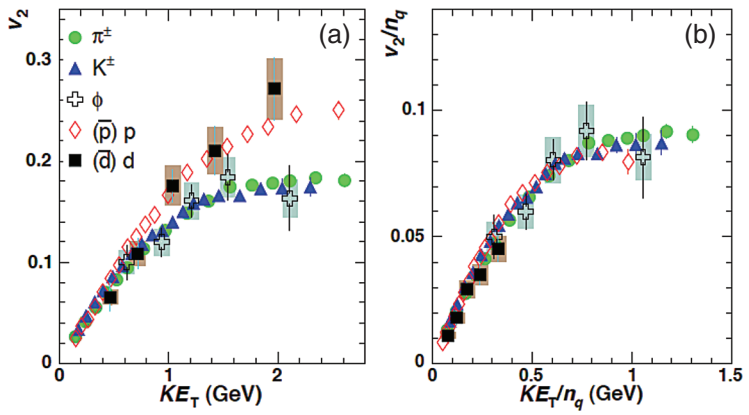

Fig. 12. $\pi^\pm$, $K^\pm$, ϕ, $(\bar{p})p$, and $(\bar{d})d$ v_2 in $\sqrt{s_{NN}} = 200$ GeV Au + Au collisions [10].

in $\sqrt{s_{NN}} = 200$ GeV Au + Au collisions. The η acceptances for each detector are as follows: RXN_{io} ($|\eta| = 1.0$–2.8), RXN_o ($|\eta| = 1.0$–1.5), RXN_i ($|\eta| = 1.5$–2.8), MPC ($|\eta| = 3.1$–3.7), and BBC ($|\eta| = 3.1$–3.9). The rapidity gap dependences are clearly visible, especially in peripheral collisions and in the higher p_T region [7].

The different analysis methods to extract v_2 are tested, where the various measured v_2 parameters with the two- and four-particle cumulant methods as well as the participant- (BBC) and spectator- (ZDC-SMD) event-plane methods are compared in Fig. 10 [8], including the results from the STAR experiment in order to investigate the non-flow and the flow fluctuation. The results from the four-particle cumulant method and spectator-event-plane method are found to give about 10–20% smaller values than the other two methods.

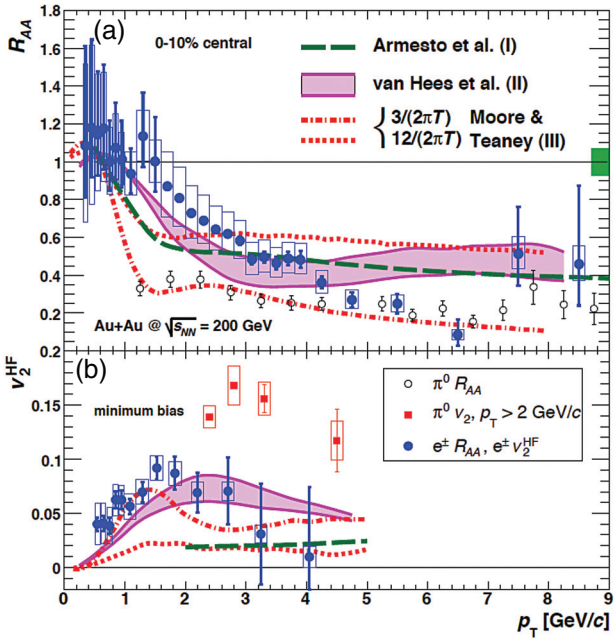

Fig. 13. R_{AA}, v_2 of an electron from heavy flavor decay [11].

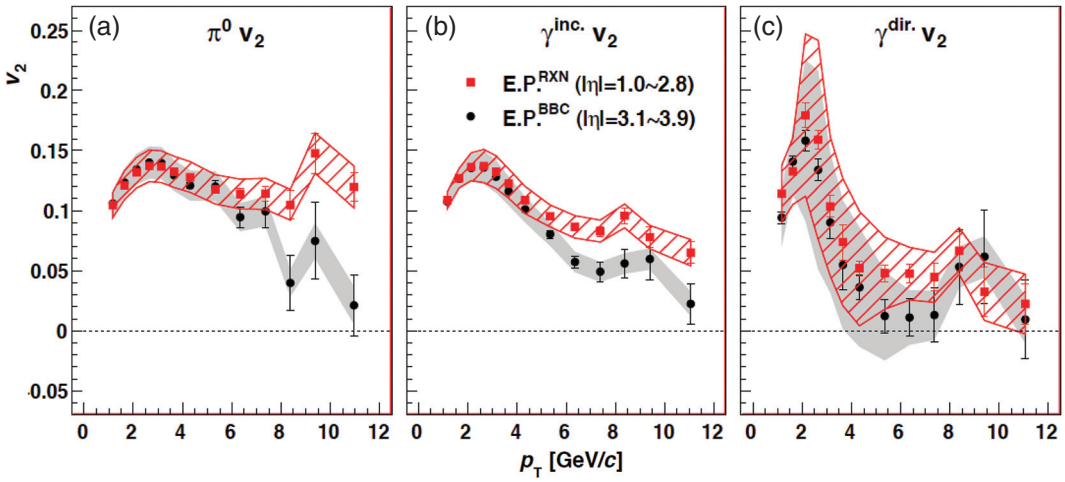

Fig. 14. π^0, inclusive photon, and direct photon v_2 [12].

The event-plane correlations between higher harmonic orders are shown in Fig. 11; panels (a) and (b) show correlations between the same order planes and panels (c) and (d) show those between different order planes. The significant Ψ_2–Ψ_2 correlation originates from the strong elliptic event anisotropy; the correlation with the true reaction plane Ψ_1–Ψ_2 and the correlation between the second- and fourth-order planes Ψ_2–Ψ_4 are also known to be significant in heavy-ion collisions. A significant even (rapidity-symmetric) contribution from v_3 is observed, which is supposed to originate from the initial geometrical fluctuation of participants, while a small but finite odd (rapidity-antisymmetric) contribution from v_3 is clearly seen [9].

The measured v_2 of $\pi^{\pm}$, $K^{\pm}$, ϕ, $(\bar{p})p$, and $(\bar{d})d$ are shown as a function of $KE_T = m_T - m_0$ transverse kinetic energy in the left panel of Fig. 12, and the quark-scaled v_2 number of these particles is shown as a function of the quark-scaled transverse kinetic energy number in the right panel of

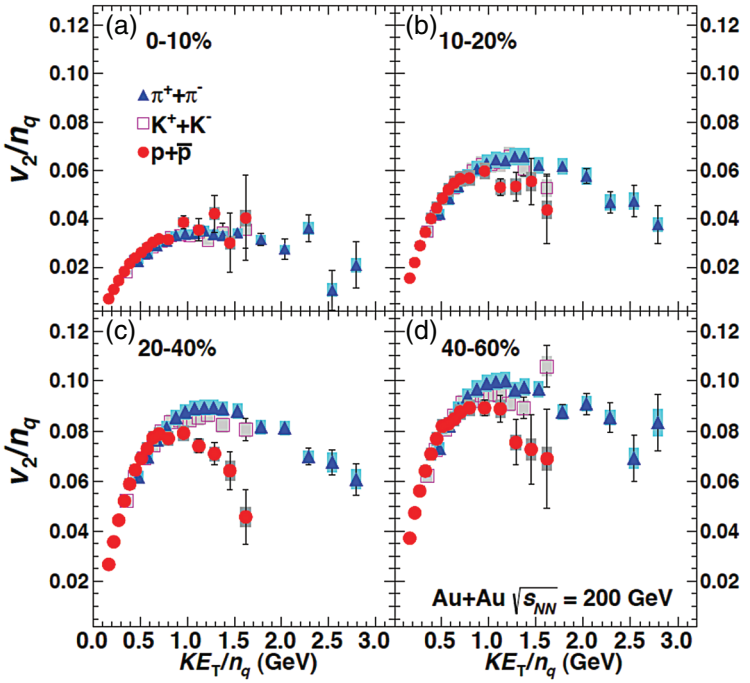

Fig. 15. Breaking of v_2/n_q scaling [13].

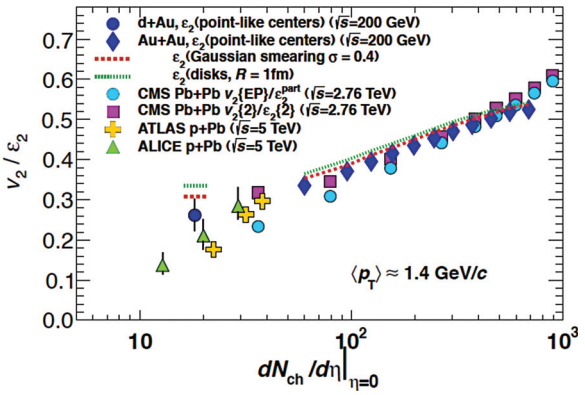

Fig. 16. v_2/ϵ_2 for d + Au and Au + Au [14].

Fig. 12. The success of the quark number-scaling of v_2 leads to the quark coalescence mechanism for hadron formation from the expanding partonic system, which can be attributed to the existence of the partonic phase before the hadronic stage [10].

Figures 13 and 14 show v_2 of an electron from heavy flavor decay, π^0, inclusive photon, and direct photon. The significant suppression and elliptic flow of a heavy flavored electron similar to the light hadrons indicate a strongly interacting quark and gluon system during the partonic phase [11]. The v_2 difference between π^0 and the inclusive photon has been used to extract the direct photon v_2. The extracted direct photon v_2 is found to be consistent with zero at high p_T, which is expected from the small interaction of prompt photons inside the QGP, while the v_2 of a thermal photon in the lower p_T region is observed to be as large as that from a hadron, which indicates the strong contribution of a later stage during the partonic stage after acquiring a large enough elliptic expansion [12].

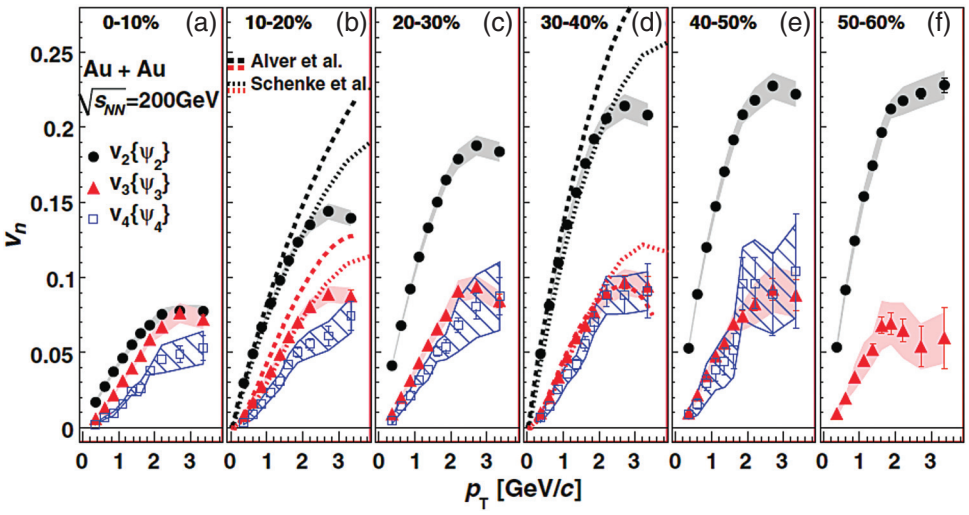

Fig. 17. $v_2\{\Psi_2\}$, $v_3\{\Psi_3\}$, and $v_4\{\Psi_4\}$ in $\sqrt{s_{NN}} = 200$ GeV Au + Au collisions [9].

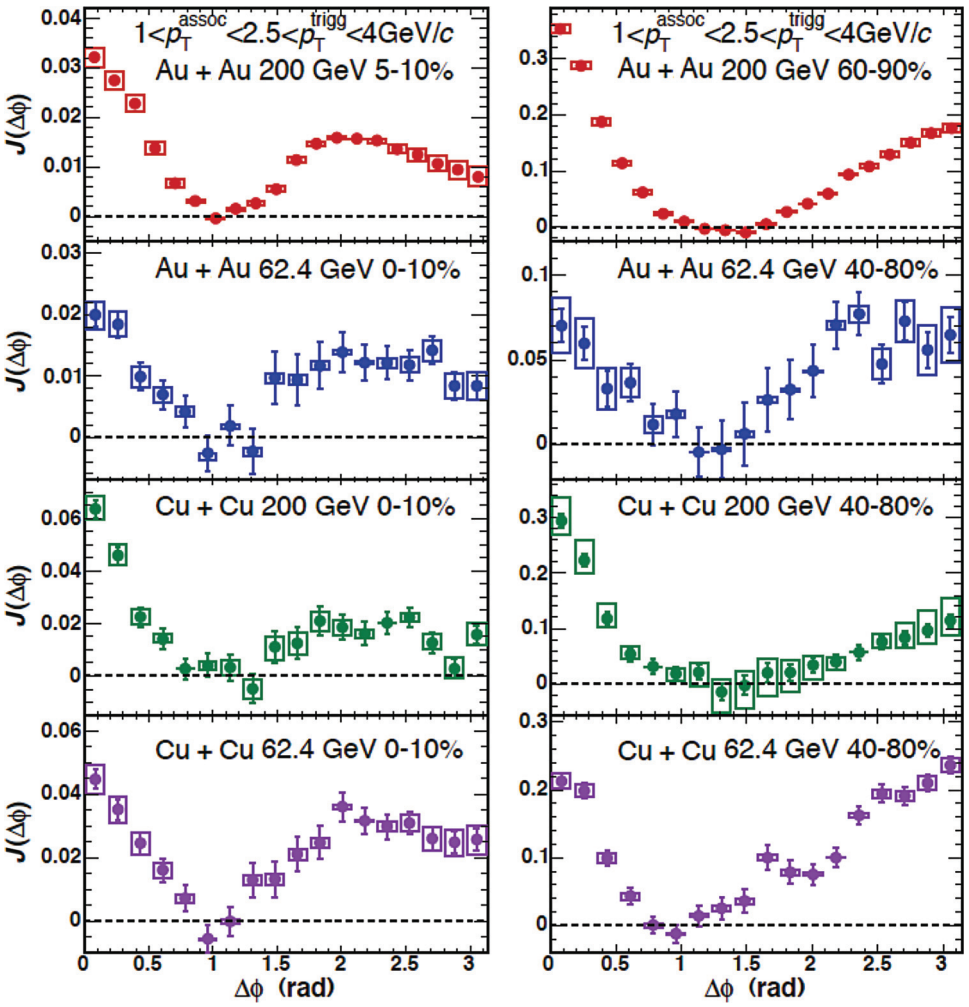

Fig. 18. Beam energy, system size, and centrality dependence of the di-hadron correlation [15].

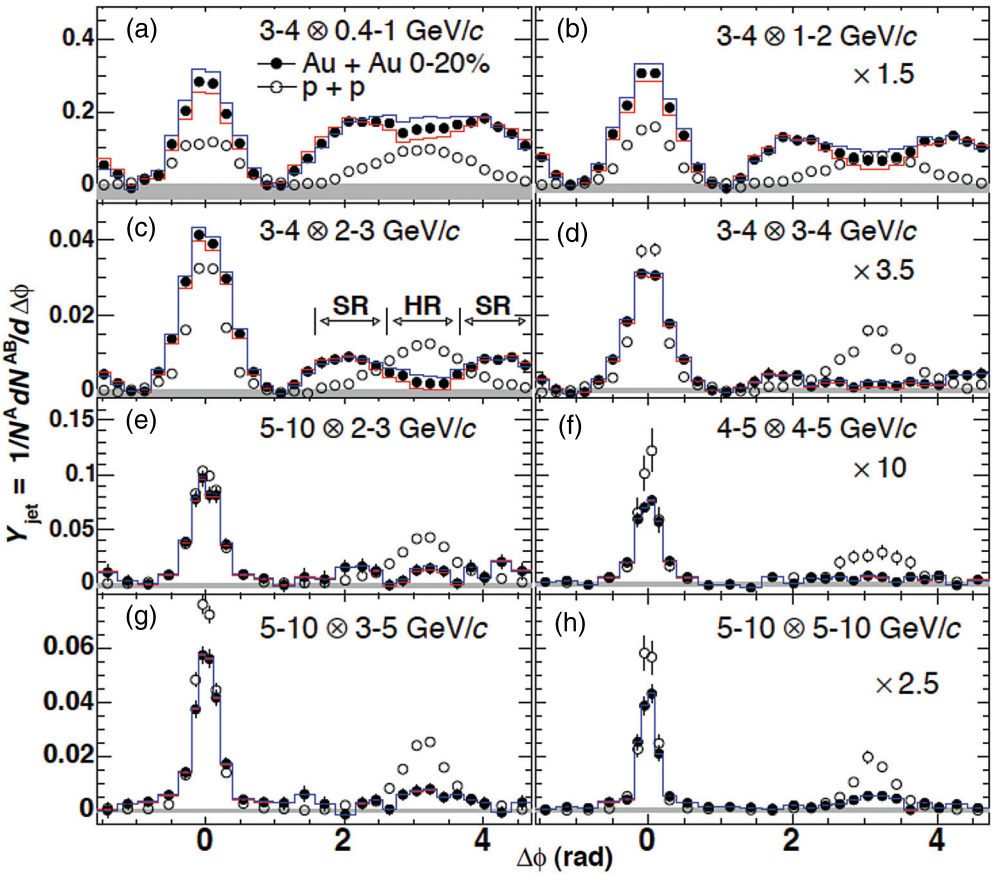

Fig. 19. p_{T} dependence of the di-hadron correlation [16].

Figures 15 and 16 show the deviation from the quark number-scaling of v_2 in the higher p_{T} region and the similarity of ϵ_2-scaled v_2 between peripheral Au + Au collisions and d + Au collisions. The breaking of the quark number-scaling of v_2 is found to happen at about $K\,E_{\mathrm{T}} \sim 0.7$ GeV [13], indicating a different mechanism such as partonic energy loss with the path-length dependence given by the elliptic geometry of the QGP. The initial geometrical eccentricity scaling of v_2 is found to describe the smooth connection from the centrality dependence observed in Au + Au collisions down to a small system such as the d + Au collision, where the mechanism of forming the elliptic expansion can be surprisingly similar in both d + Au and Au + Au collisions [14]. This might indicate that a small but high-temperature and high-pressure system is formed in d + Au collisions just as in $A + A$ collisions.

Figure 17 shows $v_2\{\Psi_2\}$, $v_3\{\Psi_3\}$, and $v_4\{\Psi_4\}$ measurements in $\sqrt{s_{NN}} = 200$ GeV Au + Au collisions, which mainly originate from the initial geometrical fluctuation; therefore, this is the dominant even (rapidity-symmetric) contribution for v_3, and $v_4\{\Psi_4\}$ is also significantly larger than $v_4\{\Psi_2\}$, especially in central collisions. The simultaneous description of v_2 and v_3 has refined the constraint for determining the initial conditions and viscosity of the plasma [9].

5. Di-hadron correlation, jet modification, and medium response

Figures 18 and 19 show the di-hadron azimuthal correlation between trigger and associate particles. The system size (Au + Au and Cu + Cu collisions) and beam energy (200 GeV and 62.4 GeV) dependence as well as the centrality dependence are shown in Fig. 18 [15]. The p_{T} dependence and a comparison with the p+p results are shown in Fig. 19 [16].

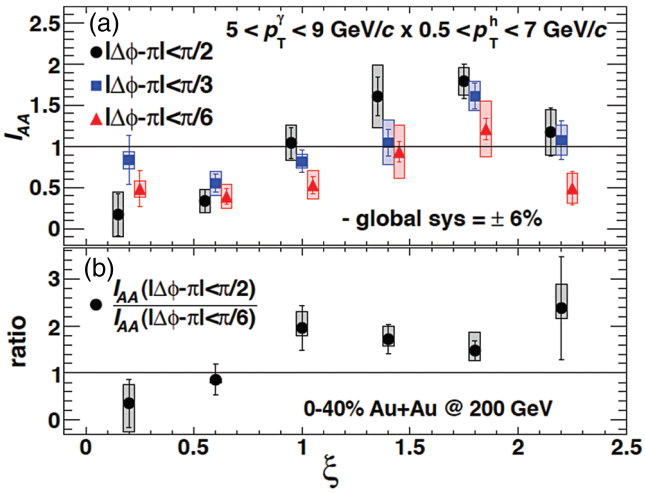

Fig. 20. Energy loss and redistribution in the γ^{direct}-hadron correlation [17].

These analyses have been performed by subtracting the flow background shape based on the $v_2\{\Psi_2\}$ and $v_4\{\Psi_2\}$ measurements, while the recent studies including higher-order event anisotropy like $v_3\{\Psi_3\}$ and $v_4\{\Psi_4\}$ indicate that the extracted shapes are largely different from the results shown here. In particular, the size of the away-side shoulder region has been significantly reduced in recent analyses. However, the transitions of the extracted correlation shape from peripheral to central collisions as well as from high p_T to low p_T are still found to be significant, which suggests a strong interplay between hard and soft processes: the high p_T suppression from the partonic energy loss and the low p_T enhancement from the redistribution of the lost energy. This has also been clearly observed in the γ^{direct}-hadron correlation, especially with low p_T particle emission at a wide angle relative to the away-side axis from the γ^{direct} trigger, as shown in Fig. 20 [17].

6. Conclusion

Selected results for soft physics from the PHENIX experiment from RHIC-BNL are reviewed and the implications on the properties of high-temperature and high-density nuclear matter from the extracted results are discussed. As a result, high-temperature and high-density nuclear matter seems to have a partonic degree of freedom, to be strongly interacting, and part of a strongly expanding partonic system such as the quark–gluon plasma. While the hard physics results will be discussed further in a separate article in this volume, the coupling and interplay of these soft and global properties with hard probes are getting more and more attention, as discussed in the last chapter, and are yet to be explored in order to understand the full nature of this plasma.

Acknowledgements

We thank the staff of the Collider–Accelerator and Physics Departments at BNL and the PHENIX Collaboration for their vital contributions. We also acknowledge support from MEXT and JSPS KAKENHI Grant Number 25105504.

References

[1] S. S. Adler et al. (PHENIX Collaboration), Phys. Rev. C **71**, 034908 (2005).
[2] S. S. Adler et al. (PHENIX Collaboration), Phys. Rev. C **69**, 034909 (2004).
[3] A. Adare et al. (PHENIX Collaboration), Phys. Rev. C **88**, 024906 (2013).

[4] S. Afanasiev et al. (PHENIX Collaboration), Phys. Rev. Lett. **103**, 142301 (2009).
[5] S. Afanasiev et al. (PHENIX Collaboration), Phys. Rev. Lett. **100**, 232301 (2008).
[6] S. S. Adler et al. (PHENIX Collaboration), Phys. Rev. Lett. **94**, 232302 (2005).
[7] A. Adare et al. (PHENIX Collaboration), Phys. Rev. Lett. **105**, 062301 (2010).
[8] S. Afanasiev et al. (PHENIX Collaboration), Phys. Rev. C **80**, 024909 (2009).
[9] A. Adare et al. (PHENIX Collaboration), Phys. Rev. Lett. **107**, 252301 (2011).
[10] S. Afanasiev et al. (PHENIX Collaboration), Phys. Rev. Lett. **99**, 052301 (2007).
[11] A. Adare et al. (PHENIX Collaboration), Phys. Rev. Lett. **98**, 172301 (2007).
[12] A. Adare et al. (PHENIX Collaboration), Phys. Rev. Lett. **109**, 122302 (2012).
[13] A. Adare et al. (PHENIX Collaboration), Phys. Rev. C **85**, 064914 (2012).
[14] A. Adare et al. (PHENIX Collaboration), Phys. Rev. Lett. **111**, 212301 (2013).
[15] A. Adare et al. (PHENIX Collaboration), Phys. Rev. Lett. **98**, 232302 (2007).
[16] A. Adare et al. (PHENIX Collaboration), Phys. Rev. C **77**, 011901 (2008).
[17] A. Adare et al. (PHENIX Collaboration), Phys. Rev. Lett. **111**, 032301 (2013).